

Estimation of Exoplanetary Planet-to-Star Radius Ratio with Homomorphic Processing

Rodrigo Mahu^a, Patricio Rojo^b, Ali Dehghan Firoozabadi^c, Ismael Soto^c, Elyar Sedaghati^d, Nestor Becerra Yoma^{a,*}

^a*Department of Electrical Engineering, Universidad de Chile, Av. Tupper 2007, Santiago, Chile*
^b*Departamento de Astronomía, Universidad de Chile, Camino el Observatorio 1515, Las Condes, Santiago, Chile*

^c*Electrical Engineering Dept., Universidad de Santiago de Chile, Ave. Ecuador 3519, Zip Code: 9170124, Santiago, Chile*

^d*European Southern Observatory, Alonso de Cordova 3107, Santiago, Chile*

Abstract

In this paper a homomorphic filtering scheme is proposed to improve the estimation of the planet/star radius ratio in astronomical transit signals. The idea is to reduce the effect of the short-term earth atmosphere variations. A two-step method is presented to compute the parameters of the transit curve from both the unfiltered and filtered data. A Monte Carlo analysis is performed by using correlated and uncorrelated noise to determine the parameters of the proposed FFT filter. The method is tested with observations of WASP-19b and WASP-17b obtained with the FORS2 instrument at the Very Large Telescope (VLT). The multi parametric fitting and the associated errors are obtained with the JKTEBOP software. The results with the white light of the exo-planet data mentioned above suggest that the homomorphic filtering can lead to substantial relative reductions in the error bars as high as 45.5% and 76.9%, respectively. The achieved reductions in the averaged error bars per channel were 48.4% with WASP-19b and 63.6% with WASP-17b. Open source MATLAB code to run the method proposed here can be downloaded from <http://www.cmrsp.cl>. This code was used to obtain the results presented in this paper.

Keywords: Exoplanet atmosphere detection, Homomorphic Processing, FFT filtering

1. Introduction

Astronomical observations have greatly benefited from the introduction of digital detectors. The migration from analogue photographic-plate detectors to digital array of pixels such as the classic charge-coupled-devices (CCDs) happened towards the end of the previous century. The much enhanced sensitivity and robustness of the digital devices permitted giant leaps in observational astronomy. However, data analysis in astronomy may still greatly benefit from signal processing techniques.

*Corresponding author

Email address: nbecerra@ing.uchile.cl (Nestor Becerra Yoma)

Preprint submitted to Astronomy and Computing

February 7, 2022

The first exoplanet around a main sequence star was detected two decades ago (Mayor and Queloz, 1995). In the short period since that discovery, the field of exoplanetary research has evolved beyond detection, where atmospheric and interior characterization of these alien worlds have been made. A multi-wavelength time-series observation of an exoplanetary transit with sufficient baseline allows for the measurement of the transmission signature of stellar light’s tangential path along the planetary terminator; likewise, an equivalent observation of an exoplanetary occultation facilitates the measurement of the emission spectrum from planet’s dayside. For both complementary methods, the depth of the feature in the lightcurve is the parameter that, after adequate modeling, relates to the exoplanetary atmospheric properties like composition, temperature-pressure profiles e.g. (Madhusudhan and Seager, 2009; Fortney et al., 2010; Iro and Deming, 2010); in the case of transits, the depth is related to the planet-to-star radius ratio.

Given the extra distortion by the Earth’s atmosphere (telluric effects), early exoatmosphere characterization was possible only through space-based instrumentation, e.g. (Charbonneau et al., 2002; Vidal-Madjar et al., 2004, 2003) by detecting wavelength-dependent variations of transit depth in a time-series spectral observations as the planet crosses in front of the host star. More troublesome became securing the first ground-based observations; after several null results e.g. (Richardson et al., 2003; Rojo, 2006) the first bona-fide detections of exoatmospheres were only possible in 2008 (Redfield et al., 2008; Snellen et al., 2008). Those first detections observed the single target star correcting the telluric effects by out-of-transit baselines, an approach that later kept yielding detection of new atomic species as in (Astudillo-Defru and Rojo, 2013).

However, simultaneously observing one or more reference stars together with the exoplanetary system has been the favored method that, complementing space-based measurements, have shown the large diversity of exoplanetary atmospheres (Bean et al., 2011; Mancini et al., 2014; Jordán et al., 2013, among others). Other ground-based methods with mixed success involve searching for the planetary spectral lines as they Doppler-wobble with respect to the telluric lines (Barnes et al., 2010; Rodler et al., 2012, 2013; Cubillos et al., 2011).

In this paper, we will study the effect on the measurement of radius-ratio in an exoplanetary lightcurve after a filtered homomorphic process. Section 2 presents the model, Section 3 applies the model to a real exoplanetary dataset for validation, Section 4 presents the results, and Section 5 presents the concluding remarks.

2. Homomorphic Processing

The main motivation of homomorphic processing is to separate signals that have been combined not additively but instead through, for instance, convolution or multiplication. This is achieved by mapping this original system onto a different space. For instance, homomorphic deconvolution and cepstral (frequency analysis in logarithmic space) analysis have been applied successfully in a variety of areas including speech and audio processing, geophysics, radar, medical imaging, and others (Oppenheim and Schaffer, 2004; Oppenheim, 1969; Sreenivasan et al., 2015, among others).

In this paper we apply homomorphic processing to separate the flux from the star of the target exoplanetary system and a simultaneously-observed flux from a reference star in the same field of view, and later filter out some of the telluric-induced high frequency

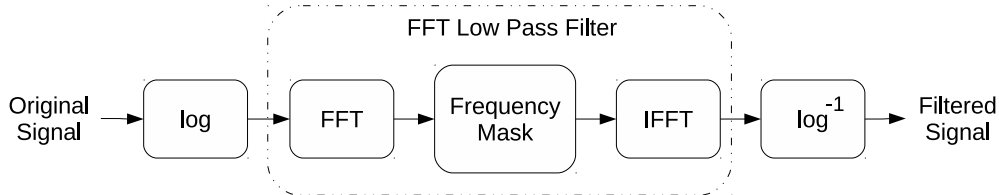


Figure 1: Block diagram of the proposed homomorphic filtering technique to improve the estimation accuracy of the radius-ratio

components from the data. By doing so, we seek to improve the accuracy of the exoplanet radius-ratio estimation. Figure 1 shows the proposed homomorphic filtering scheme.

2.1. Model

The observed flux from the star with the transiting planet (F_T) for each λ (wavelength) is modeled as follows:

$$F_T(\lambda, t) = F_{TO}(\lambda, t) \times A_E(\lambda, t) + n_T(\lambda, t) \quad (1)$$

and the corresponding observed flux for the reference (F_R) star can be expressed as:

$$F_R(\lambda, t) = F_{RO}(\lambda) \times A_E(\lambda, t) + n_R(\lambda, t) \quad (2)$$

where $F_{TO}(\lambda, t)$ and $F_{RO}(\lambda)$ denote the original flux without the telluric effects for the target and reference star, respectively; $A_E(\lambda, t)$ corresponds to the telluric atmosphere response; and, $n_T(\lambda, t)$ and $n_R(\lambda, t)$ indicate the observation noise for the target and reference stars. Also, the original flux from the reference star, $F_{RO}(\lambda)$, is independent of time.

The transit light curve for a given λ , $F_{TO}(\lambda, t)$, is described by the Mandel & Agol model (Mandel and Agol, 2002). The flux received from the target star depends on the radiated energy, which is a function of λ , and on the exoatmosphere absorption during the planetary transit that also depends on λ . In the case of the reference star we can assume that there is no time dependency.

The telluric effect on the flux received from the target and reference stars, $A_E(\lambda, t)$, is the standard attenuation term ($\propto e^{-\tau}$). This component is wavelength and time dependent as the atmosphere changes. Atmosphere perturbations can be classified as long- or short-term. The air mass changes slowly in a few-hour observation window as the star moves in the sky. In contrast, parameters such as density, pressure and amount of water may present rapid fluctuations on timescales of 10 or 15 minutes.

The additive observation noise is composed of a white and a red noise component. Both types of noise present high frequency energies, although they are more significant in the white noise.

2.2. Mapping

We study homomorphic mapping into logarithmic space by first applying the logarithm operator to the observed light fluxes in (1) and (2) to transform the multiplication to addition:

$$\begin{aligned} \log [F_T(\lambda, t)] &= \log [F_{TO}(\lambda, t)] + \log [A_E(\lambda, t)] \\ &+ \log \left[1 + \frac{n_T(\lambda, t)}{F_{TO}(\lambda, t)A_E(\lambda, t)} \right] \end{aligned} \quad (3)$$

$$\begin{aligned} \log [F_R(\lambda, t)] &= \log [F_{RO}(\lambda)] + \log [A_E(\lambda, t)] \\ &+ \log \left[1 + \frac{n_R(\lambda, t)}{F_{RO}(\lambda)A_E(\lambda, t)} \right] \end{aligned} \quad (4)$$

By considering that $F_{TO}(\lambda, t)A_E(\lambda, t) \gg n_T(\lambda, t)$ and $F_{RO}(\lambda)A_E(\lambda, t) \gg n_R(\lambda, t)$, we can make use of the approximation $\log(1 + x) \approx x$, if $x \ll 1$. The normalization of $F_T(\lambda, t)$ with respect to $F_R(\lambda, t)$, i.e. the subtraction of (4) from (3), can then be expressed as:

$$\begin{aligned} \log \left[\frac{F_T(\lambda, t)}{F_R(\lambda, t)} \right] &= \log [F_{TO}(\lambda, t)] - \log [F_{RO}(\lambda)] \\ &+ \frac{n_T(\lambda, t)}{F_{TO}(\lambda, t)A_E(\lambda, t)} - \frac{n_R(\lambda, t)}{F_{RO}(\lambda)A_E(\lambda, t)} \end{aligned} \quad (5)$$

where the component $\log [A_E(\lambda, t)]$ in (3) and (4) are canceled out since the target and the reference star's angular separation on the sky is negligible.

2.3. Filtering

The flux ratio (5) is thus processed with a low-pass Fast Fourier Transform (FFT) filter to suppress or reduce the high frequency components of the noise terms. Basically, the main idea is to reduce the distortion caused by the short term variations of the telluric response and of the observation noise. If the attenuated components are faster than the transit time, then a more accurate estimation of the radius ratio could be achieved.

The low-pass filter is applied in the frequency domain to prevent the addition of delay and phase distortion of the frequency components. The resulting filter is non-causal and requires processing the whole signal at once. This is achieved by multiplying the FFT spectrum with a frequency mask that attenuates all the components above a cut off frequency. Figure 2 shows the low-pass filter mask defined by the cut-off frequency (COF) and the rejection band gain (RBG) in dB. Then, the inverse FFT is employed to come back to the time domain. Finally, after low-pass filtering the log of the normalized transit flux curve, the inverse logarithm operator is applied.

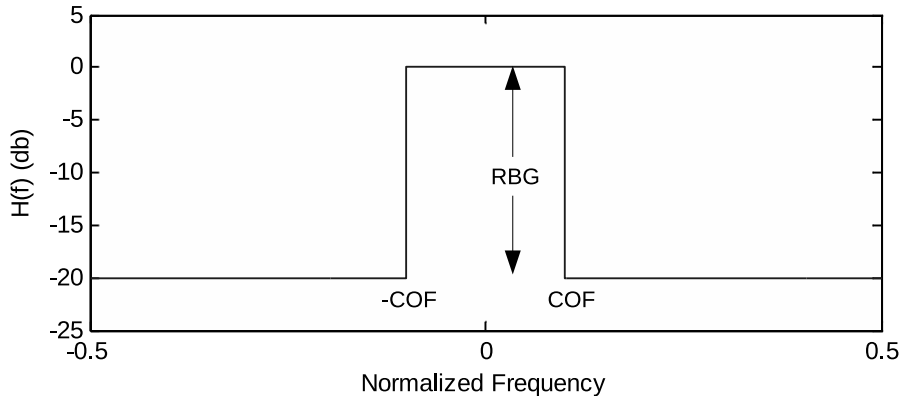


Figure 2: FFT Low-pass filter mask defined by the cut-off frequency (COF) and the rejection band gain (RBG).

2.4. Parameter estimation

We follow the standard prescription of Mandel and Agol (2002) to find the best-fit parameters to the data. Since for characterizing extrasolar atmospheres, it is typically required to have a precision better than 10^{-3} of the incoming flux. It is important to verify that new methods do not add unwanted systematic effects that could offset the measurement. In fact, our early tests did show that a low-pass filtering distorts the shape of the lightcurve for the estimation of some of the parameters (most greatly for the sum of radii and the inclination).

Therefore, in order to counteract the above-mentioned distortion induced by the homomorphic low-pass filter, and since the most relevant parameter for exoatmospheric measurements is the radius-ratio, we develop a two-step method (Fig. 3) that only tries to fit this parameter, while minimizing errors associated to possible degeneracies with other parameters. First, the observed transit curve is fitted with the Mandel & Agol model. In this paper this is achieved by using JKTEBOP (Southworth, 2013). As a result the fitted parameters are estimated and the radius ratio coefficient is discarded. Second, the homomorphic low-filtering is applied and the resulting curve is also fitted with the Mandel & Agol model. However, in contrast to the previous step, the Mandel & Agol fitting makes use of all the parameters previously estimated except radius ratio, which is now determined (Table 1).

3. Validation

3.1. The Data

We evaluated the proposed method with the transit time series corresponding to planets WASP-19b (Sedaghati et al., 2015) and WASP-17b (Sedaghati et al., 2016). The WASP-19b and WASP-17b data were obtained on the nights of Nov 16, 2014, and Jun 18, 2015, respectively, using FORS2 at the VLT with Grism 600RI. In the case of WASP-19b, $30'' \times 10''$ slits were used on six reference stars, in addition to WASP-19, and the

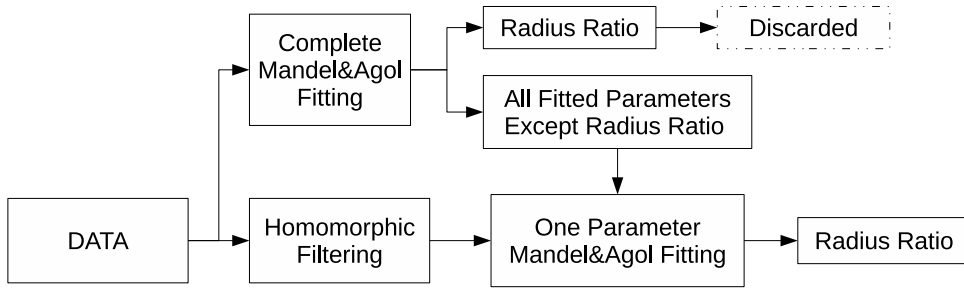


Figure 3: Diagram for the two-step method of estimation.

Table 1: Parameters from the Mandel and Agol (2002) prescription that are fit during the two-step method

Parameter Name	Fit to curve	
	unfiltered	filtered
radius ratio	✓	✓
radii sum	✓	
inclination	✓	
linear limb darkening	✓	
quadratic limb darkening	✓	
period	✓	
mid transit	✓	

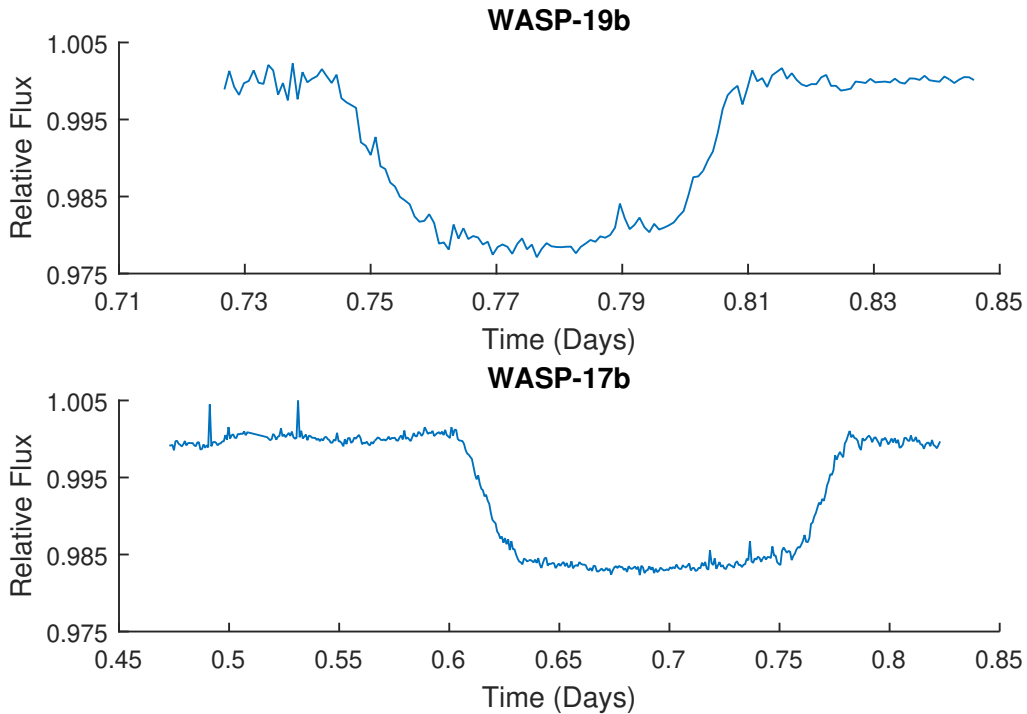


Figure 4: White light data from WASP-19 (top) and WASP-17 (bottom). The curves were obtained by summing all the spectral channels from 535nm to 837nm and from 570nm to 790nm for WASP-19b and WASP-17b, respectively. Finally, the curves were normalized by the flux average of the reference star.

exposure time was 30s. For WASP-17b, $30'' \times 15''$ slits were employed on five reference stars, in addition to WASP-17, and the exposure time was 35s (Fig. 4).

3.2. Monte Carlo-based estimation method

To estimate the parameters of the proposed homomorphic FFT filter, we generated a set of artificial 1000 transit noisy signals for each planet considered here, i.e. WASP-19b and WASP-17b. This dataset was produced by adopting the following procedure: first, a synthetic transit curve was obtained for each planet with the Mandel & Agol model by making use of the estimated transit parameters of WASP-19b and WASP-17b according to (Sedaghati et al., 2015) and (Sedaghati et al., 2016), respectively; then, white noise and red noise were added to the synthetic transit curves. The red noise used here presents a spectral density distribution that decreases at a rate of f^{-2} (Carter and Winn, 2009). The red and white noise power were the same. The resulting SNR after the addition of both types of noise was equal to the SNR of the white light curves shown in Figure 4. Figure 5 depicts example of the noisy transit curves generated for WASP-19b and WASP-17b. The grid search described in Subsection 3.3 was employed to estimate the homomorphic FFT filter parameters, i.e. COF and RBG.

Figure 6 shows the Monte Carlo-based estimation method. The 1000 noisy signals were filtered with the homomorphic low-pass filter. Then JKTEBOP was used to es-

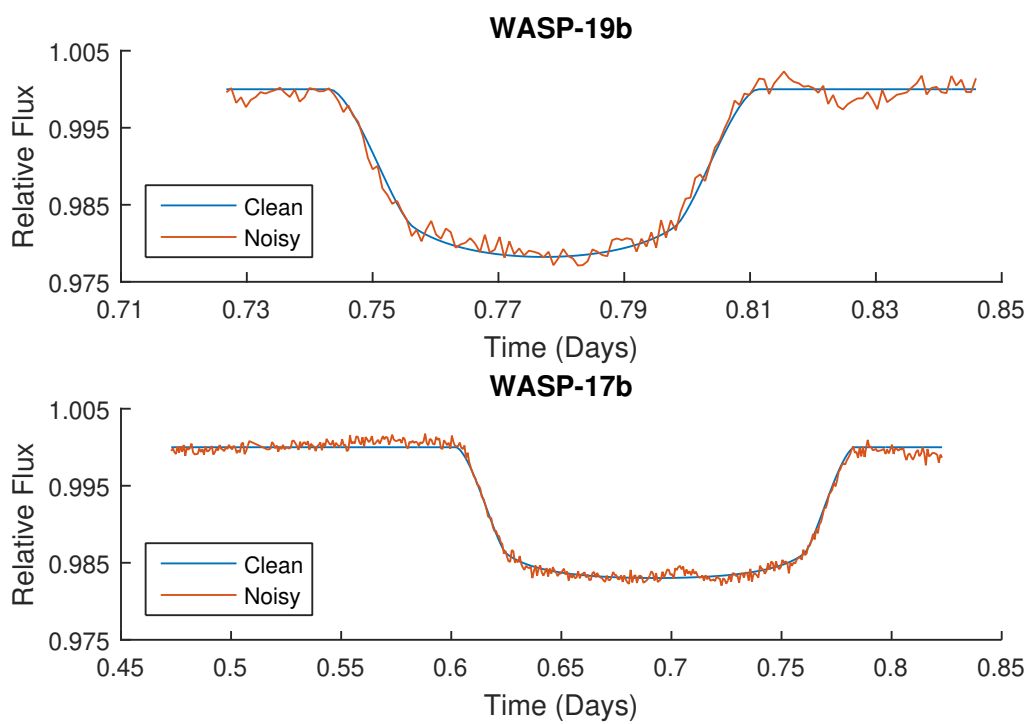


Figure 5: Examples of artificially generated noisy transit curves employed in the Monte Carlo simulations: WASP-19b (top) and WASP-17b (bottom).

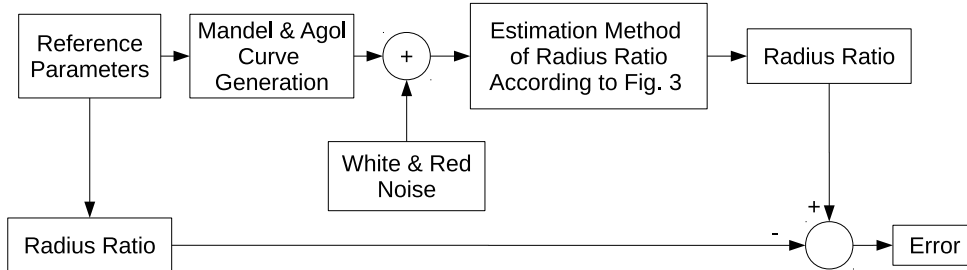


Figure 6: Monte Carlo simulation to estimate the parameters of the homomorphic FFT filter.

estimate the transit parameters for the unfiltered and filtered signals. After estimating the parameters with the original 1000 unfiltered and filtered signals, we calculated the average estimation of radius ratio and corresponding error bar considering an interval of 68% of confidence that corresponds to one gaussian standard deviation.

As can be seen in Figure 7, in the early test (i.e. fitting all parameters after the filter), the homomorphic low-pass filter led to a reduction of 45.4% in the estimation of error bar for the radius ratio with WASP-19b. However, the method is unable to find the correct estimation for inclination and radii sum, and the error bar of the mid transit increased, because of the distortion incorporated by the homomorphic low-pass filter in the transit curve transition.

As can be seen in Fig. 8, the early test with WASP-17b leads to a low error reduction of 1.69 %, which is much lower than the error reduction achieved with WASP-19b. This result must be due to the fact that, according to Table 2, the white light curve of WASP-17b provides an SNR that is 77% higher than the one observed in the WASP-19b light curve when the noise signal is obtained as the residual of the JKTEBOP estimation. In contrast, Table 2 also shows that the SNR averaged across all the channels is just 20% higher in WASP-17b than in WASP-19b. This apparent contradiction is explained as follows. According to Table 4, the noise in WASP-17b is much less correlated between channels than in WASP-19b. Consequently, when the residual noise signals are summed over all the channels, the resulting noise energy is much lower with WASP-17b than with WASP-19b. Coefficient Q in Table 4 is defined as the quotient of the energy of the signal resulting from the summation of all the channel noises by the summation of the individual channel noise energies as in Eq. 6 (see Table 3):

$$Q = \frac{\sum_t [Noise(t)]^2}{\sum_\lambda \sum_t [Noise(t, \lambda)]^2} \quad (6)$$

where $Noise(t, \lambda)$ denote sample t of the noise signal at channel λ and,

$$Noise(t) = \sum_\lambda Noise(t, \lambda) \quad (7)$$

Accordingly, WASP-17b delivers a Q value that is 3.5 times lower than the one obtained with WASP-19b.

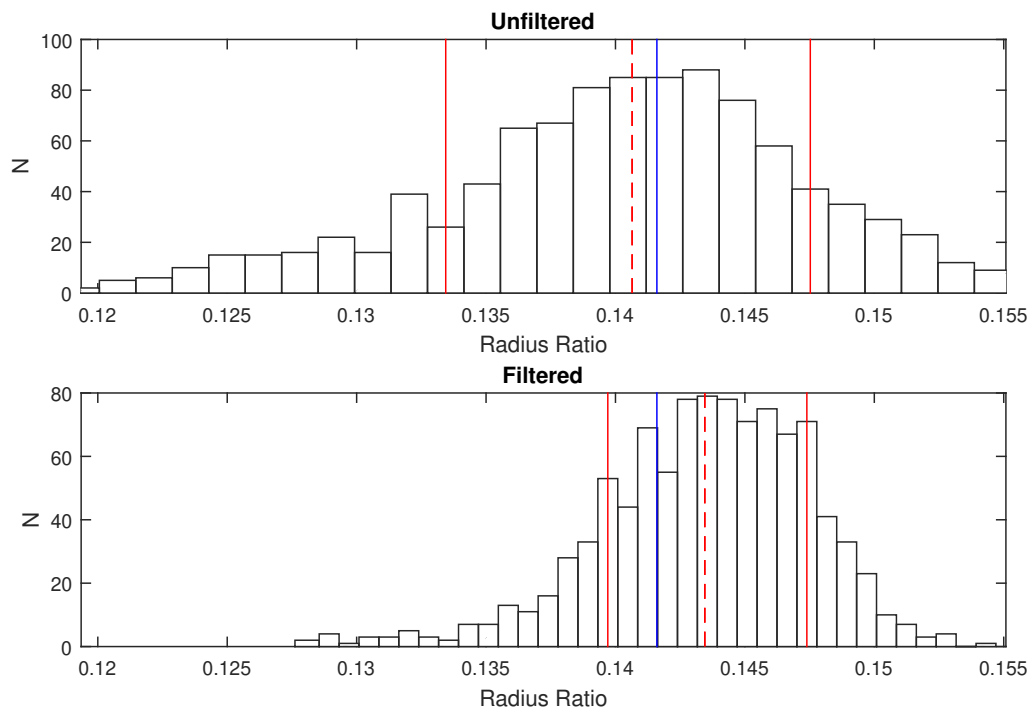


Figure 7: Histograms of the estimated radius-ratio for WASP-19b with the early test: unfiltered (top) and filtered (bottom) data. The red continuous lines, at the outer sides of the histogram, bound the 68% confidence interval. The blue and dashed red lines, in the middle of the histogram, indicate the reference radius-ratio and the average estimation, respectively. (For interpretation of the references to colour in this figure legend, the reader is referred to the web version of this article.)

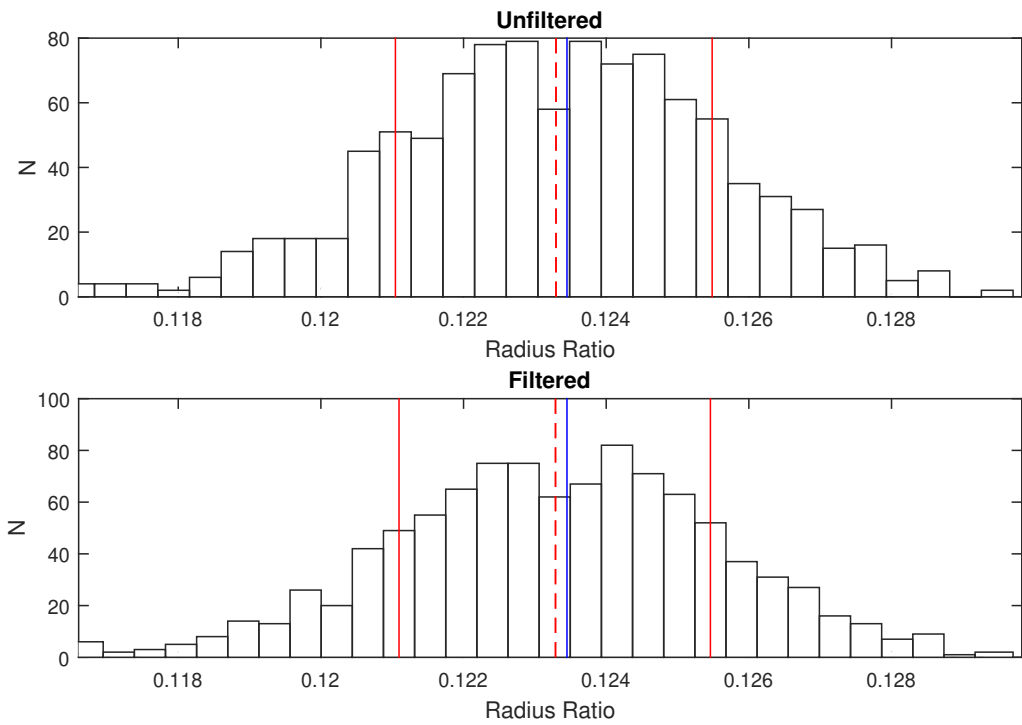


Figure 8: Histograms of the estimated radius-ratio for WASP-17b with the early test: unfiltered (top) and filtered (bottom) data. The red continuous lines, at the outer sides of the histogram, bound the 68% confidence interval. The blue and dashed red lines, in the middle of the histogram, indicate the reference radius-ratio and the average estimation, respectively. (For interpretation of the references to colour in this figure legend, the reader is referred to the web version of this article.)

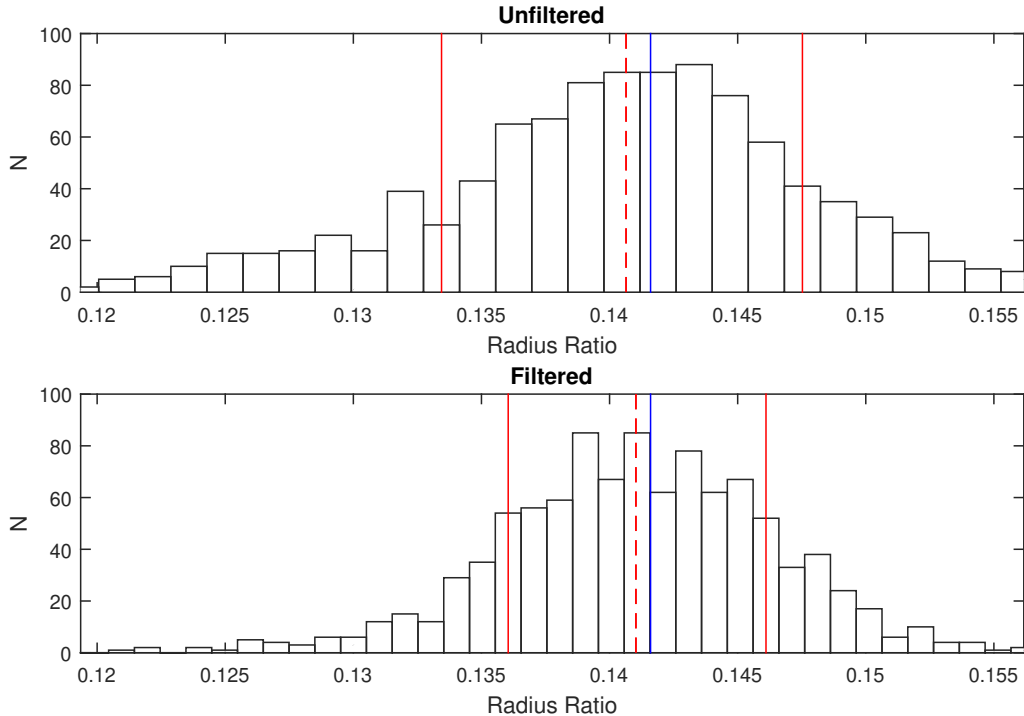


Figure 9: Histograms of the estimated radius ratio for WASP-19 with the proposed estimation method: unfiltered (top) and filtered (bottom) data. The red continuous lines, at the outer sides of the histogram, bound the 68% confidence interval. The blue and dashed red lines, in the middle of the histogram, indicate the reference radius-ratio and the average estimation, respectively. (For interpretation of the references to colour in this figure legend, the reader is referred to the web version of this article.)

Results are shown in Fig. 9 for the proposed two-step method. The reduction in the estimation error bar for WASP-19 was as high as 28.4% without additional distortion. Fig. 10 shows an improvement of 0.66% for the case of WASP-17.

3.3. Filter optimization

The homomorphic FFT low-pass filter defined in Figs. 1 and 2 has two parameters that need to be tuned, COF and RBG. These parameters were optimized by making use of a two-dimensional grid search methodology. In the case of WASP-19b, 153 samples, the 256 FFT was obtained and the optimal COF was searched in the integer interval [1, 127]. The optimal RBG is found within the set [10dB, 20dB, 30dB, 40dB, 50dB, 60dB, 70dB, 80dB]. For each pair (COF, RBG) the Monte Carlo simulation, described in Subsection 3.2, was performed and the optimal pair (COF, RBG) was determined with respect to the lowest interval of 68% confidence that includes the correct radius ratio. Accordingly, the optimal filter parameters for WASP-19b are: for the early test, COF equal to five FFT samples and RBG equal to 10dB; and, for the proposed method, COF corresponds to 14 FFT samples and RBG is equal to 30dB. The WASP-17b data contains 477 samples and the 512 FFT was computed. To adopt a similar resolution to WASP-19b, the homomorphic FFT low-pass filter for WASP-17b was optimized by searching

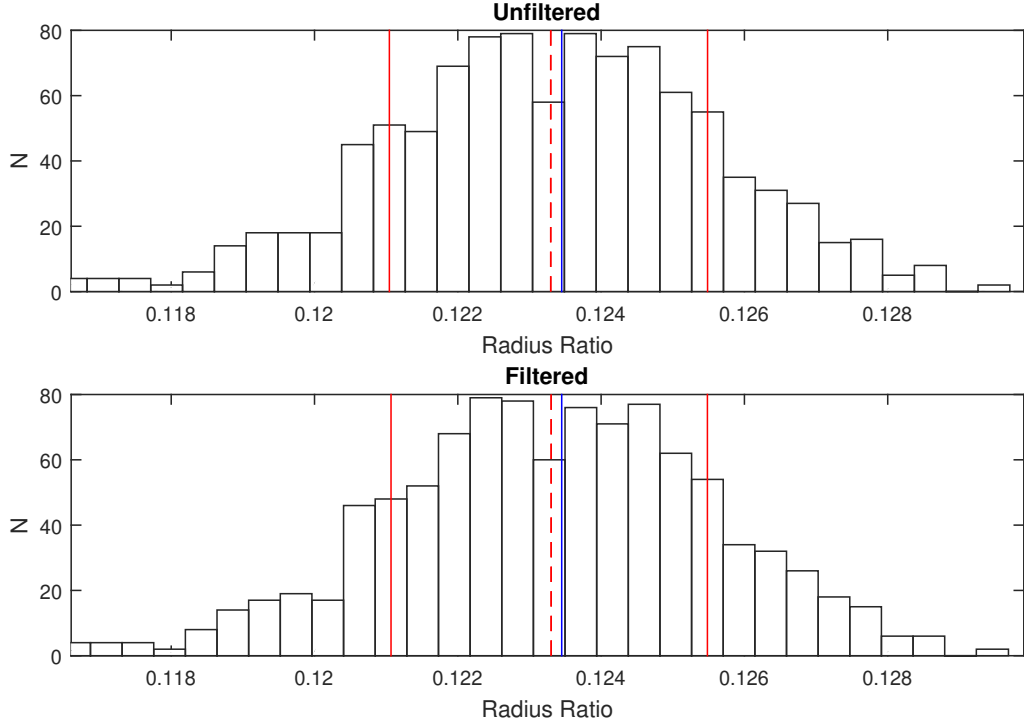


Figure 10: Histograms of the estimated radius ratio for WASP-17 with the proposed estimation method: unfiltered (top) and filtered (bottom) data. The red continuous lines, at the outer sides of the histogram, bound the 68% confidence interval. The blue and dashed red lines, in the middle of the histogram, indicate the reference radius-ratio and the average estimation, respectively. (For interpretation of the references to colour in this figure legend, the reader is referred to the web version of this article.)

Table 2: SNR in the white light curves and the SNR averaged over all the channels with WASP-17b and WASP-19b. The noise is estimated as the residual between the real signal and the JKTEBOP estimation of the transit curve.

Planet Name	White light curve SNR	SNR averaged over all the channels
WASP-17b	147.99	74.75
WASP-19b	83.45	62.30

Table 3: SNR at each channel with WASP-17b and WASP-19b. The noise is estimated as the residual between the real signal and the JKTEBOP estimation of the transit curve.

WASP 17b		WASP 19b	
Channel	SNR	Channel	SNR
570.00 nm	12.25	560.00 nm	57.02
580.00 nm	27.07	570.00 nm	52.57
590.00 nm	63.05	581.00 nm	53.21
600.00 nm	83.91	590.00 nm	58.70
610.00 nm	94.11	601.00 nm	61.17
620.00 nm	82.24	610.00 nm	65.24
630.00 nm	79.32	620.00 nm	67.52
640.00 nm	85.83	630.00 nm	64.09
650.00 nm	95.70	640.50 nm	60.31
660.00 nm	99.10	650.00 nm	61.87
670.00 nm	111.27	660.50 nm	62.94
680.00 nm	118.00	670.00 nm	63.95
690.00 nm	99.97	681.25 nm	67.56
700.00 nm	93.96	690.00 nm	69.80
710.00 nm	98.89	701.25 nm	64.27
720.00 nm	83.70	711.25 nm	57.97
730.00 nm	81.65	720.00 nm	57.44
740.00 nm	84.22	731.25 nm	49.19
750.00 nm	60.62	740.00 nm	59.50
760.00 nm	34.58	748.00 nm	73.07
770.00 nm	34.16	760.00 nm	45.15
780.00 nm	47.20	768.00 nm	51.08
790.00 nm	48.41	780.00 nm	74.46
		790.00 nm	72.17
		800.00 nm	73.82
		810.00 nm	71.10
		820.00 nm	66.99

Table 4: Correlation coefficient between channel noises averaged across all the channels and metric Q according to (6) with WASP-17b and WASP-19b.

Comparison Criteria	Planet Name	
	WASP-17b	WASP-19b
Average correlation coefficient of the noise between channels.	0.4521	0.7309
Q, as defined in (6).	0.0431	0.1513

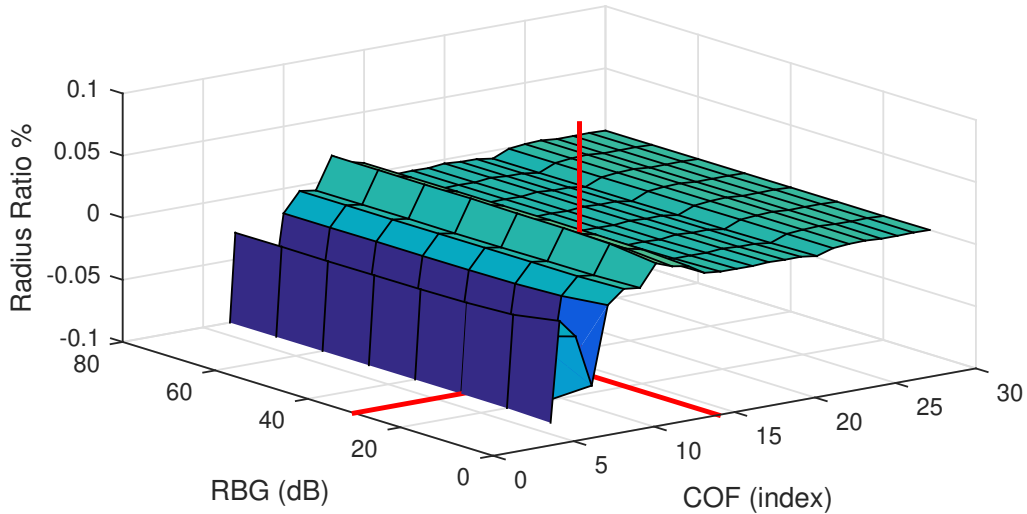


Figure 11: Evaluation of the distortion introduced in the original clean transit curve by the proposed method. The error curves were obtained when radius-ratio was made equal to 0.1416. The filtered radius-ratios were estimated with JKTEBOP. The optimal filter (COF=14 FFT samples and RBG=30 dB) is indicated by the red lines. (For interpretation of the references to colour in this figure legend, the reader is referred to the web version of this article.)

COF in the interval $[1, 255]$ and discarding one every two FFT samples. Accordingly, the optimal filter parameters for WASP-17b are: for the early test, COF equal to 159 FFT samples and RBG equal to 40dB; and, for the proposed method, COF corresponds to 15 FFT samples and RBG is equal to 10dB.

Distortion analysis

The distortion introduced by the proposed method and its dependence on filter parameters was evaluated by processing the clean transit curves with the scheme shown in Fig.1 by applying the optimal FFT low-pass filter with COF=14 FFT samples and RBG=30dB. The clean transit curves were generated by using the parameters from WASP-19b and varying radius-ratio. The procedure was repeated with six radius-ratios representative of real exoatmospheric modulation along a typical spectrum: 0.136, 0.138, 0.14, 0.1416, 0.142 & 0.144. Then, the error between the radius-ratios in the original clean and filtered transit curves is computed. Figure 11 shows the error curve when radius-ratio was made equal to 0.1416. As can be seen in Fig. 11, there is a wide range of values for COF and RBG, including the optimal ones, where the error is lower than 10^{-4} . The same behavior is obtained with the other five reference radius-ratios. This result strongly suggests that the proposed homomorphic filtering does not introduce any significant distortion into the observed original transit curves

4. Results

We used JKTEBOP with the white light from WASP-19b and WASP-17b to compare the ordinary estimation of the transit curve parameters (baseline) with the one

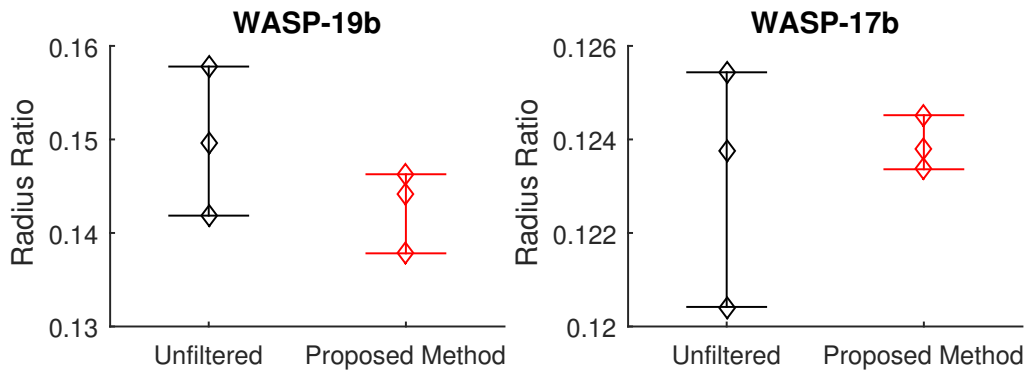


Figure 12: Estimation of radius ratio on white light data: black, unfiltered; and, red, with the proposed method. (For interpretation of the references to colour in this figure legend, the reader is referred to the web version of this article.)

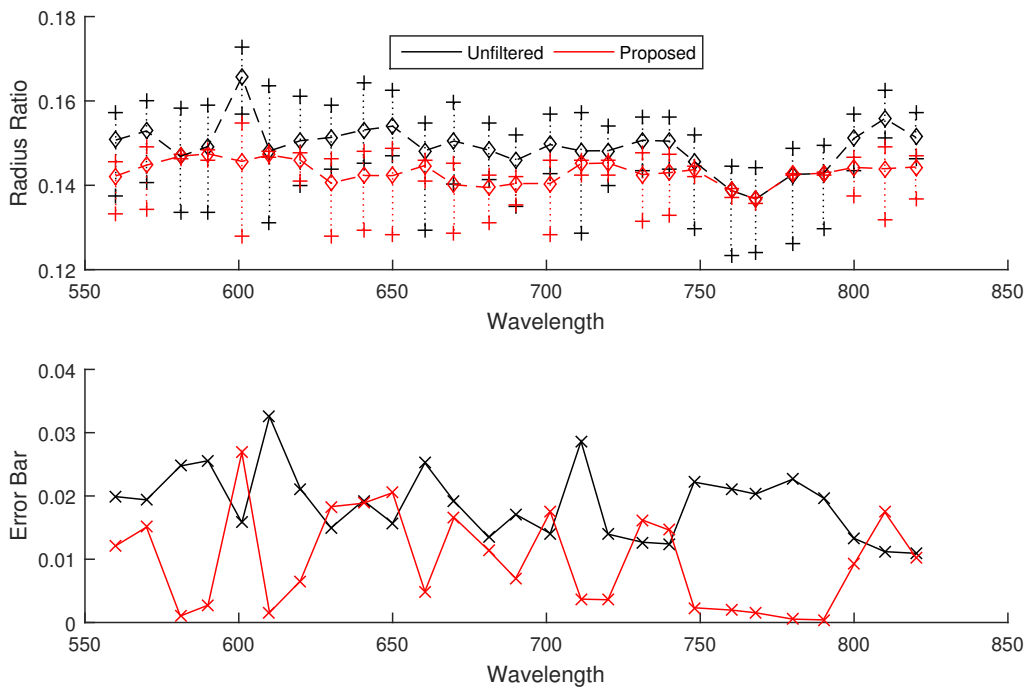


Figure 13: Estimations of radius-ratio with the corresponding confidence intervals by employing JKTE-BOP: black, unfiltered data; red, proposed homomorphic filtering method. The wavelength channels are defined in (Sedaghati et al., 2015) for WASP-19b. (For interpretation of the references to colour in this figure legend, the reader is referred to the web version of this article.)

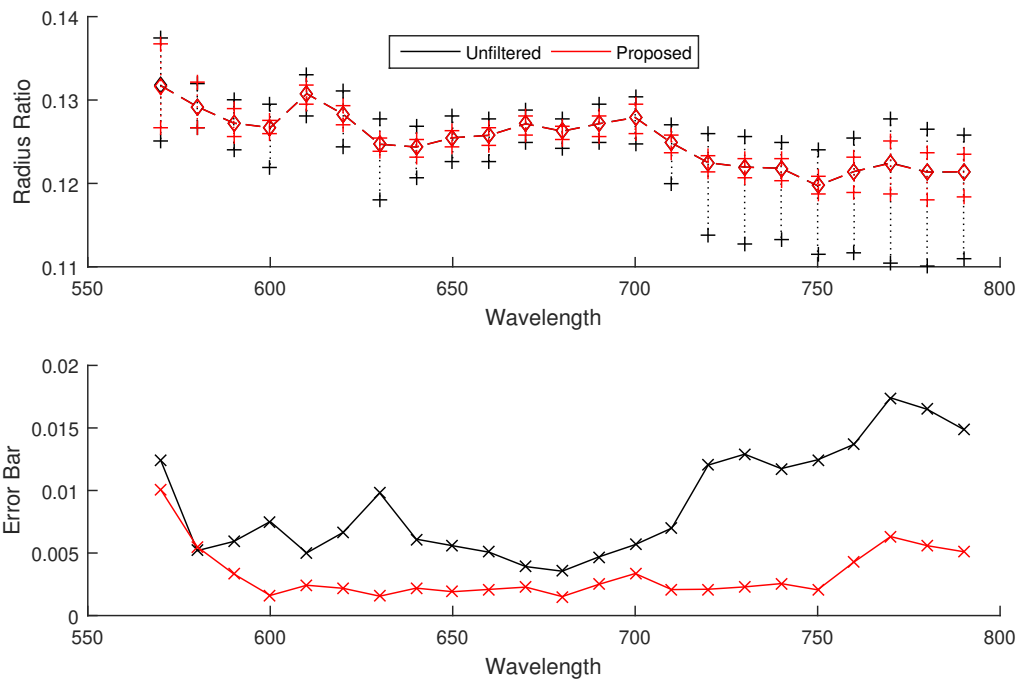


Figure 14: Estimations of radius-ratio with the corresponding confidence intervals by employing JKTE-BOP: black, unfiltered data; red, proposed homomorphic filtering method. The wavelength channels are defined in (Sedaghati et al., 2016) for WASP-17b. (For interpretation of the references to colour in this figure legend, the reader is referred to the web version of this article.)

obtained by making use of the proposed method (see Fig. 12). According to Fig. 12, the radius ratios for WASP-19b and WASP-17b are consistent because there is a clear intersection between the error intervals obtained with the ordinary baseline processing and the one achieved with the proposed method. Nevertheless, the homomorphic filtering delivers error intervals that are 45.5% and 76.9% smaller for WASP-19b and WASP-17b, respectively.

Figure 13 shows the radius ratios computed by employing the proposed restricted estimation method with the 27 channels of WASP-19 reported in (Sedaghati et al., 2015). As can be seen in Fig. 13, both sets of estimated radius ratios are also consistent but the proposed method provided error bars that are 48.4% lower in average than without filtering. A similar analysis results from Figure 14 where the radius ratios obtained with the 23 channels of WASP-17, according to (Sedaghati et al., 2016), were estimated with and without the proposed homomorphic filtering. As can be seen in Figure 14, a dramatic average reduction of 63.6% in the error bars was achieved with WASP-17b.

5. Conclusions

The homomorphic filtering technique proposed here is applied to improve the estimation of the radius ratio in astronomical transit signals. The main motivation is to reduce the interference from the short-term earth atmosphere variations. The parameters of the homomorphic FFT filter are estimated with a Monte Carlo-based scheme. The proposed method was tested with the white light of WASP-19b and WASP-17b real data using JKTEBOP, and was able to lead to dramatic reductions of 45.5% and 76.9% in the error bars, respectively. Similar reductions in the averaged error bars per channel were achieved with WASP-19b and WASP-17b: 48.4% and 63.6%, respectively. Moreover, the sensibility analysis shows that the distortion caused by the technique is lower than the target precision, i.e. 0.1%. Finally, the application of the homomorphic filtering scheme to additional exo-planet real data is proposed as a future research.

Acknowledgements

The research leading to these results was funded by CONICYT-ANILLO project ACT 1120, project POSTDOC_DICYT (No.041613DA_POSTDOC), Universidad de Santiago de Chile (USACH).

References

References

- Astudillo-Defru, N., Rojo, P., 2013. Ground-based detection of calcium and possibly scandium and hydrogen in the atmosphere of HD 209458b. *A&A* 557, A56. doi:10.1051/0004-6361/201219018, arXiv:1306.5475.
- Barnes, J.R., Barman, T.S., Jones, H.R.A., Barber, R.J., Hansen, B.M.S., Prato, L., Rice, E.L., Leigh, C.J., Collier Cameron, A., Pinfield, D.J., 2010. A search for molecules in the atmosphere of HD 189733b. *MNRAS* 401, 445–454. doi:10.1111/j.1365-2966.2009.15654.x, arXiv:0909.2510.
- Bean, J.L., Désert, J.M., Kabath, P., Stalder, B., Seager, S., Miller-Ricci Kempton, E., Berta, Z.K., Homeier, D., Walsh, S., Seifahrt, A., 2011. The Optical and Near-infrared Transmission Spectrum of the Super-Earth GJ 1214b: Further Evidence for a Metal-rich Atmosphere. *ApJ* 743, 92. doi:10.1088/0004-637X/743/1/92, arXiv:1109.0582.

- Carter, J.A., Winn, J.N., 2009. Parameter estimation from time-series data with correlated errors: a wavelet-based method and its application to transit light curves. *The Astrophysical Journal* 704, 51.
- Charbonneau, D., Brown, T.M., Noyes, R.W., Gilliland, R.L., 2002. Detection of an Extrasolar Planet Atmosphere. *ApJ* 568, 377–384. doi:10.1086/338770, arXiv:astro-ph/0111544.
- Cubillos, P.E., Rojo, P., Fortney, J.J., 2011. High-resolution spectroscopic search for the thermal emission of the extrasolar planet HD 217107 b. *A&A* 529, A88. doi:10.1051/0004-6361/201015802, arXiv:1103.3039.
- Fortney, J.J., Shabram, M., Showman, A.P., Lian, Y., Freedman, R.S., Marley, M.S., Lewis, N.K., 2010. Transmission Spectra of Three-Dimensional Hot Jupiter Model Atmospheres. *ApJ* 709, 1396–1406. doi:10.1088/0004-637X/709/2/1396, arXiv:0912.2350.
- Iro, N., Deming, L.D., 2010. A Time-Dependent Radiative Model for the Atmosphere of the Eccentric Exoplanets. *ApJ* 712, 218–225. doi:10.1088/0004-637X/712/1/218.
- Jordán, A., Espinoza, N., Rabus, M., Eyheramendy, S., Sing, D.K., Désert, J.M., Bakos, G.Á., Fortney, J.J., López-Morales, M., Maxted, P.F.L., Triaud, A.H.M.J., Szentgyorgyi, A., 2013. A Ground-based Optical Transmission Spectrum of WASP-6b. *ApJ* 778, 184. doi:10.1088/0004-637X/778/2/184, arXiv:1310.6048.
- Madhusudhan, N., Seager, S., 2009. A Temperature and Abundance Retrieval Method for Exoplanet Atmospheres. *ApJ* 707, 24–39. doi:10.1088/0004-637X/707/1/24, arXiv:0910.1347.
- Mancini, L., Southworth, J., Ciceri, S., Dominik, M., Henning, T., Jørgensen, U.G., Lanza, A.F., Rabus, M., Snodgrass, C., Vilela, C., Alsubai, K.A., Bozza, V., Bramich, D.M., Calchi Novati, S., D’Ago, G., Figuera Jaimes, R., Galianni, P., Gu, S.H., Harpsøe, K., Hinse, T., Hundertmark, M., Juncher, D., Kains, N., Korhonen, H., Popovas, A., Rahvar, S., Skottfelt, J., Street, R., Surdej, J., Tsapras, Y., Wang, X.B., Wertz, O., 2014. Physical properties and transmission spectrum of the WASP-80 planetary system from multi-colour photometry. *A&A* 562, A126. doi:10.1051/0004-6361/201323265, arXiv:1312.4982.
- Mandel, K., Agol, E., 2002. Analytic light curves for planetary transit searches. *The Astrophysical Journal Letters* 580, L171.
- Mayor, M., Queloz, D., 1995. A jupiter-mass companion to a solar-type star. *NATURE* 378, 23.
- Oppenheim, A.V., 1969. Speech analysis-synthesis system based on homomorphic filtering. *The Journal of the Acoustical Society of America* 45, 458–465.
- Oppenheim, A.V., Schaffer, R.W., 2004. From frequency to quefrency: A history of the cepstrum. *Signal Processing Magazine, IEEE* 21, 95–106.
- Redfield, S., Endl, M., Cochran, W.D., Koesterke, L., 2008. Sodium Absorption from the Exoplanetary Atmosphere of HD 189733b Detected in the Optical Transmission Spectrum. *ApJ* 673, L87–L90. doi:10.1086/527475, arXiv:0712.0761.
- Richardson, L.J., Deming, D., Wiedemann, G., Goukenleuque, C., Steyert, D., Harrington, J., Esposito, L.W., 2003. Infrared Observations during the Secondary Eclipse of HD 209458b. I. 3.6 Micron Occultation Spectroscopy Using the Very Large Telescope. *ApJ* 584, 1053–1062. doi:10.1086/345813.
- Rodler, F., Kürster, M., Barnes, J.R., 2013. Detection of CO absorption in the atmosphere of the hot Jupiter HD 189733b. *MNRAS* 432, 1980–1988. doi:10.1093/mnras/stt462.
- Rodler, F., Lopez-Morales, M., Ribas, I., 2012. Weighing the Non-transiting Hot Jupiter τ Boo b. *ApJ* 753, L25. doi:10.1088/2041-8205/753/1/L25, arXiv:1206.6197.
- Rojo, P.M., 2006. Transit spectroscopy of the extrasolar planet HD 209458B: The search for water. Ph.D. thesis. Cornell University.
- Sedaghati, E., Boffin, H., Csizmadia, S., Gibson, N., Kabath, P., Mallonn, M., Van den Ancker, M., 2015. Regaining the fors: optical ground-based transmission spectroscopy of the exoplanet wasp-19b with vlt+ fors2. *Astronomy & Astrophysics* 576, L11.
- Sedaghati, E., Boffin, H.M., Jeřabková, T., Muñoz, A.G., Grenfell, J.L., Smette, A., Ivanov, V.D., Csizmadia, S., Cabrera, J., Kabath, P., et al., 2016. Potassium detection in the clear atmosphere of a hot-jupiter-fors2 transmission spectroscopy of wasp-17b. *Astronomy & Astrophysics* 596, A47.
- Snellen, I.A.G., Albrecht, S., de Mooij, E.J.W., Le Poole, R.S., 2008. Ground-based detection of sodium in the transmission spectrum of exoplanet HD 209458b. *A&A* 487, 357–362. doi:10.1051/0004-6361:200809762, arXiv:0805.0789.
- Southworth, J., 2013. The solar-type eclipsing binary system ll aquarii. *Astronomy & Astrophysics* 557, A119.
- Sreenivasan, K.R., Havlicek, M., Deshpande, G., 2015. Nonparametric hemodynamic deconvolution of fmri using homomorphic filtering. *Medical Imaging, IEEE Transactions on* 34, 1155–1163.
- Vidal-Madjar, A., Désert, J.M., Lecavelier des Etangs, A., Hébrard, G., Ballester, G.E., Ehrenreich, D., Ferlet, R., McConnell, J.C., Mayor, M., Parkinson, C.D., 2004. Detection of Oxygen and Carbon

in the Hydrodynamically Escaping Atmosphere of the Extrasolar Planet HD 209458b. *ApJ* 604, L69–L72. doi:10.1086/383347.

Vidal-Madjar, A., Lecavelier des Etangs, A., Désert, J.M., Ballester, G.E., Ferlet, R., Hébrard, G., Mayor, M., 2003. An extended upper atmosphere around the extrasolar planet HD209458b. *Nature* 422, 143–146.